Journal of Ovonic Research Vol. 21, No. 5, September - October 2025, p. 591 - 603

Laser synthesis and photocatalytic properties of ultrasmall TiO_2 anchored ZnO core-shell nanoparticles

Z. Liu [a,*], K. Li [b], R. X. Wang [a]
[a] *School of Science, Jinling Institute of Technology, Nanjing 211168, Jiangsu, China*
[b] *Guangdong Provincial Key Laboratory of Electronic Functional Materials and Devices，Huizhou University, Huizhou 516001, Guangdong, China*

ZnO-TiO_2 core-shell nanocomposites were fabricated via laser ablation in liquid (LAL), followed by post-annealing at various temperatures. The influence of annealing temperature on the structural and optical properties, as well as the photocatalytic activity of the resulting nanocomposites, was systematically investigated using X-ray diffraction (XRD), ultraviolet-visible diffuse reflectance spectroscopy (UV-Vis DRS) for powders, and ultraviolet-visible absorption spectroscopy for dye aqueous solutions. The morphology and elemental composition were analyzed by transmission electron microscopy (TEM) and energy-dispersive spectroscopy (EDS). XRD and TEM analyses confirmed that the composites possessed excellent crystallinity and a well-defined core-shell structure, with ZnO as the central core and ultrasmall TiO_2 nanoparticles constituting the shell layer. Optical measurements showed pronounced ultraviolet absorption, with minimal variation in the optical band gap (3.30-3.32 eV) regardless of annealing temperature. The photocatalytic activity, assessed by Rhodamine B (RhB) dye degradation under ultraviolet (UV) irradiation, was significantly influenced by the annealing process, with samples annealed at 400 °C achieving the highest degradation efficiency of 73.3%. These findings demonstrate that careful control of post-annealing conditions can optimize the photocatalytic performance of ZnO-TiO_2 core-shell nanocomposites, underlining their potential in UV-driven environmental remediation applications.

(Received July 17, 2025; Accepted September 23, 2025)

Keywords: Laser ablation in liquid, Core-shell, Annealing temperature, Nanoparticles, Photocatalytic

1. Introduction

As the development of industry, environmental problem of water pollution caused by industrial wastewater has caused a serious concern worldwide [1]. Synthetic dyes are typical organic compounds, which are extensively used in textile, printing and dyeing industries [2]. These dyes presented in industrial wastewater are frequently harmful and resistant to

---

[*] Corresponding author: liuzhen@jit.edu.cn

https://doi.org/10.15251/JOR.2025.215.591

bio-degradation. The excessive usage and improper handling of wastewater containing organic dyes can present considerable risks to aquatic ecosystems and human health [3-5]. It is essential to develop water treatment technologies for removing organic dyes from wastewater. Conventional water treatment methods, such as biological processes, coagulation, and activated carbon adsorption, often fail to effectively remove dye contaminants or may lead to secondary pollution [6].

In recent decades, semiconductor photocatalysis, as an advanced oxidation process, has emerged as a highly promising and sustainable approach for degrading toxic dyes and other organic pollutants in aqueous environments [7-10]. The irradiated light with larger energy than the band gaps of semiconductors can be absorbed by the semiconductor photocatalysts and generated the photo-induced electron-hole pairs. The photo generated electrons will migrate to the conduction band, while the holes will remain in the valance band of the semiconductors. These charge carriers can participate in the redox reactions with the water and dissolved oxygen molecules, generating the reactive species [11]. With the help of the reactive species, the organic dyes can be converted into the end products, including carbon dioxide and water.

In the pursuit of developing efficient photocatalysts for dye degradation, numerous semiconductors materials, including ZnO, TiO_2, WO_3, SnO_2, CdS, and C_3N_4, have been extensively investigated by researchers [12-17]. ZnO possesses a wide bandgap energy (>3 eV), high carrier mobility and large exciton binding energy (60 meV), which enable its application in various fields such as photovoltaic cells, photodetectors, sunscreens and photocatalysis [18-22]. In the context of photocatalysis, similarly, TiO_2 is regarded as one of the most studied semiconductor materials owing to its excellent photo and chemical stability, non-toxicity, simple synthesis process and low production cost [23]. TiO_2 typically exhibits wide band gap energy, which can be activated by artificial ultraviolet or solar irradiation [13]. These characteristics render TiO_2 highly suitable for diverse applications, including environmental remediation, sterilization, water splitting, and dye degradation [24-27]. Furthermore, the integration of multiple semiconductors can not only combine the advantages of each component but also generate interfacial electric fields at their junctions, which facilitate the separation of photoinduced charge carriers and thereby enhance photocatalytic efficiency [28-30]. Therefore, it is essential to investigate the photocatalytic performance of composites containing ZnO and TiO_2.

To boost semiconductor photocatalytic properties of ZnO or TiO_2, researchers frequently modify them through ion doping, co-catalyst deposition and semiconductor coupling [9, 31, 32]. Numerous synthesis methods have been reported for preparation of ZnO or TiO_2 based photocatalysts [12, 24, 33-37]. These methods include co-precipitation [12], solvothermal [24], electrospinning [33], magnetron sputtering [34], spray pyrolysis [35], sol-gel [36], and laser ablation in liquid (LAL) [37, 38]. Among these synthetic methods, the LAL method offers significant advantages, such as the ability to produce high-purity, contamination-free catalysts without the need for organic surfactants. In addition, it enables precise control over particle size, defects and morphology, thereby supporting the synthesis of various complex structures.

Herein, laser ablation of dual-target composed of ZnO ceramics and metallic Ti was applied to synthesize ZnO-TiO_2 core-shell nanoparticles. XRD and TEM were utilized to analyze the structural and morphological features of the synthesized ZnO-TiO_2 nanocomposites. EDS Mapping was utilized to investigate the element distribution within the composite nanostructure. The optical properties of the composite nanoparticles were investigated to determine their band gap energy. The annealing temperature was optimized to obtain the best performance in photocatalytic degradation of RhB dye under UV irradiation. The results reveal that the laser ablated ultrasmall TiO_2 anchored ZnO core-shell nanoparticles annealed at 400 °C exhibit optimized photocatalytic performance.

2. Experimental procedures

2.1. Fabrication of TiO_2 anchored ZnO nanocomposites

The ultrasmall TiO_2 anchored ZnO nanocomposites were prepared via pulsed laser ablation in liquid method with deionized water serving as the liquid medium. ZnO ceramic (Thickness: 6 mm) and high pure Titanium metal ingot (99.99%, Diameter: 25.4 mm, Thickness: 6 mm) were used as solid target for laser ablation [10]. Two solid targets are fixed at the bottom of a 200 mL beaker and immersed in 50 mL of deionized water. Pulsed laser (Wavelength: 1064 nm, Duration: 100 ns, Laser power: 50 W) was focused on the surface of the targets with help of a focusing lens with focal length of 261 mm [10]. The laser spot was scanned on the surface of two targets alternately, and each scanning cycle covers 10 mm^2 rectangular area. After laser ablation for 120 min, the colloidal ZnO-TiO_2 composites were collected. For investigating the effect of annealing temperature on physicochemical properties, the colloidal composites were subjected to centrifugation, drying and annealing treatment at 300 °C, 400 °C, 500 °C for 1 h, respectively. These samples were identified as SN, S300, S400, S500 for without annealing, post-annealed at 300 °C, 400 °C, 500 °C, respectively.

2.2 Characterization of ZnO-TiO_2 nanocomposites

The structural properties of ZnO-TiO_2 nanocomposites were investigated by X-ray diffraction (XRD) measurements performed on a Bruker D8 Advance diffractometer (operating at 30 kV, 30mA, Cu Kα line, λ=0.154 nm). The scanning range of 2θ was from 20° to 80°. The characteristic diffraction peaks were used to estimate crystallize size. The morphological information was analyzed via transmission electron microscopy (TEM). The chemical composition and elemental distribution of synthesized ZnO-TiO_2 nanocomposites were investigated via Energy Dispersive Spectroscopy (EDS) Mapping. The optical properties of these nanocomposites annealed at different temperature were investigated via ultraviolet-visible (UV-Vis) diffusion reflectance spectroscopy (DRS) using a spectrometer (Shimadzu UV-3600i Plus).

The photodegradation of RhB dye in aqueous solutions were carried out under irradiation of 250 W high pressure mercury lamp in the presence of each photocatalyst. Initially, to ensure adsorption-desorption equilibrium between the dye and the catalyst, the 100 mL dye wastewater (10 mg/L) and 50 mg catalyst were mixed and stirred in the dark for 30 minutes. Subsequently, the mixed solutions were exposed to light, and were extracted 1 mL every 30 min. The extracted solutions were centrifuged at 10,000 rpm for 5 min to separate the catalysts, followed by recording the absorption spectra of dye solutions. The absorption characteristics of the solutions were analyzed using a UV-Vis spectrophotometer. The absorption intensity at 554 nm was monitored to determine the concentration of the dye.

3. Results and discussion

Fig. 1 presents the XRD patterns of ZnO-TiO_2 composites produced via laser ablation and subsequently annealed at various temperatures. It can be seen that the diffraction pattern of the laser ablated composites show obvious strong and sharp diffraction peaks, indicating the excellent crystallinity of main components. This diffraction patterns for composite powders annealed at different temperature can be well matched with JCPDS Card No. 36-1451. The diffraction peaks are identified at 31.8°, 34.5°, 36.3°, 47.6°, 56.6°, 62.9°, 66.4°, 68.1° and 69.1°, which can be indexed to the (100), (002), (101), (102), (110), (103), (200), (112) and (201) crystal planes of hexagonal wurtzite ZnO, respectively. However, no diffraction peaks for TiO_2 are observed in the XRD patterns. The absence of diffraction peaks corresponding to TiO_2 in the XRD patterns could be attributed to two possible reasons. Firstly, TiO_2 may not form a crystalline phase but instead exists in an amorphous form. This is often related to factors such as the preparation method, annealing temperature, or the distribution of TiO_2 during the fabrication process. Second reason is the content of TiO_2 is very low, its diffraction signals might be overshadowed by strong diffraction peaks from other components in the composites. It can be observed from the pattern that ZnO in the composites exhibit very strong diffraction signals, such as the major peaks near approximately 31.8°, 34.5°, and 36.3°. Therefore, even if TiO_2 is present, its signal might be too weak and easily masked by the intense peaks from ZnO. With an increase of annealing temperature, the diffraction peaks do not show significant changes, suggesting the absence of phase transformation for ZnO.

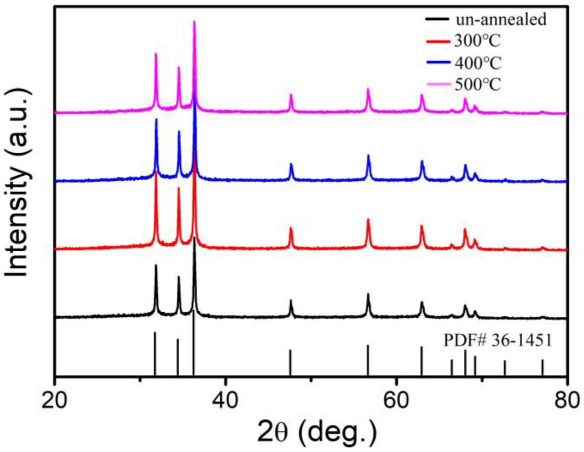

Fig. 1. XRD patterns of LAL-synthesized ZnO-TiO_2 composites annealed at different temperature.

The effect of annealing temperature on the crystalline size of LAL-synthesized ZnO-TiO_2 nanoparticles is assessed by analyzing the strongest diffraction peak associated with the (101) planes of ZnO using the XRD profiles and Scherrer equation (1) [10].

$$D = \frac{K\lambda}{\beta cos\theta} \tag{1}$$

wherein, D represents the crystalline size, K symbolizes shape factor with the value of 0.89, λ is the wavelength of X-Ray with value of 0.1542 nm, β is the full width at half maximum of diffraction peak, while θ represents the angular position of the diffraction peak [10]. The average crystalline sizes of ZnO based nanoparticles are determined to be 40.7 nm, 41.0 nm, 39.9 nm, 41.1 nm for SN, S300, S400, S500, respectively.

For evaluating the morphological characters of the prepared nanocomposites, LAL-synthesized ZnO-TiO_2 nanoparticles annealed at 400 °C were characterized via TEM. The TEM micrograph of the synthesized nanocomposites was shown in Fig. 2 (a). As illustrated, the synthesized particles are nearly spherical in shape with a core-shell structure. It can be observed that a dense and darker center is surrounded by dispersed small structures. These observations confirmed that the composite nanoparticle is composed of a larger central particle and a layer of ultrasmall particles, less than 15 nm in size, anchored on the surface of the central particle. Fig. 2 (b) displays the selected area electron diffraction (SAED) pattern of the synthesized composite nanoparticles. As shown, the SAED pattern exhibits bright diffraction spots arranged along several rings, as well as clear diffraction halo rings. The presence of discrete diffraction spots indicates that the nanocomposites possess a polycrystalline structure with good crystallinity. Furthermore, the appearance of diffraction halo rings confirms the existence of ultrasmall nanoparticles within the composite particles. Fig. 2 (c) presents the high-resolution TEM (HRTEM) image of ZnO-TiO_2 composite nanostructure. The clear and ordered lattice fringes are observed in HRTEM images, indicating that the synthesized nanoparticles are well crystallized, consistent with the XRD results. In addition, the image displays that a fraction of the ultrasmall nanoparticles aggregated around the central particle are tightly anchored to its surface with well-defined interfaces, while others aggregate together, forming connections among themselves and creating nanopores between the aggregated shell layer and the core.

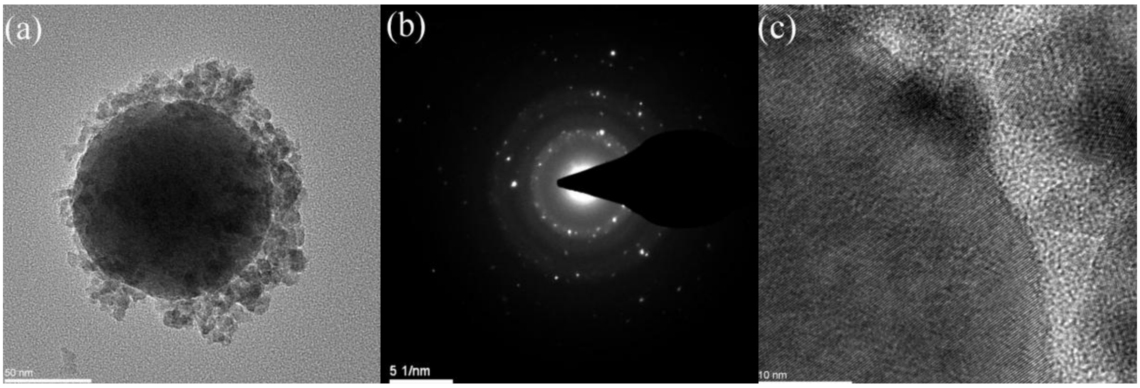

Fig. 2. (a) TEM Micrograph of laser ablated ZnO-TiO_2 nanocomposites annealed at 400 ℃，(b) SAED pattern of the nanocomposites，(c) HRTEM image of the nanocomposites.

To clearly identify the elemental composition of core-shell structured nanocomposite particles, the EDS mapping images of the sample are presented in Fig. (3). As can be seen in the comprehensive elemental distribution map of Fig. 3 (a), the presence of Zn (purple), Ti (green), O (red) elements in $ZnO\text{-}TiO_2$ composite nanoparticles are confirmed. The color distribution at the central and edge regions differs slightly, suggesting that the Zn and Ti exhibit distinct spatial distributions. The individual elemental distribution maps for Zn, Ti, and O are further presented using purple, green, and red points in Fig. 3 (b), (c), and (d), respectively. It can be found that the Zn, Ti, and O elements are uniformly distributed in the circular-like area, while the distribution areas of Zn and O elements are slightly larger than that of Ti. These results suggest that the Zn-rich region forms the core of the composite nanoparticles. Combined with the TEM micrograph in Fig. 2 (a), it can be concluded that ZnO forms the central particle and ultrasmall TiO_2 nanoparticles form the shell layer of the $ZnO\text{-}TiO_2$ core-shell structure.

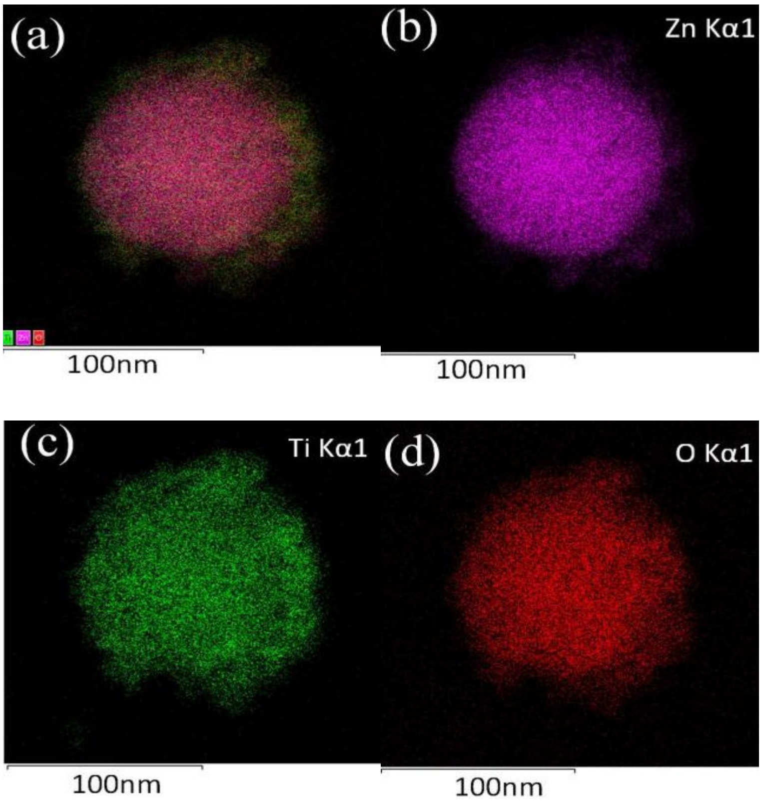

Fig. 3. EDS mapping (a) comprehensive elemental distribution map, and the individual distribution map for (b) Zn, (c) Ti, (d) O element.

Optical absorption properties of semiconductor nanocomposites are crucial for their photocatalytic performance. The UV-Vis diffuse-reflectance spectra of the laser-synthesized $ZnO\text{-}TiO_2$ core-shell nanocomposites annealed at various temperatures were measured to investigate their optical absorption properties. The optical diffuse-reflectance spectra for laser-ablated $ZnO\text{-}TiO_2$ core-shell nanocomposites without annealing and annealed at 300 °C, 400 °C, 500 °C are displayed in Fig. 4. As illustrated, all synthesized nanocomposites exhibit a substantial decrease in reflectance at wavelengths below 400 nm, implying notable ultraviolet light absorption. It is worth noting that the reflectance in visible and near-infrared range from 400 nm to 800 nm changes significantly with different annealing temperatures. As the annealing temperature increases from 300 °C to 500 °C, the reflectance in the 400 nm to 800 nm decreases, suggesting the defect density in laser-ablated nanocomposites reduces with the elevation annealing temperature [10].

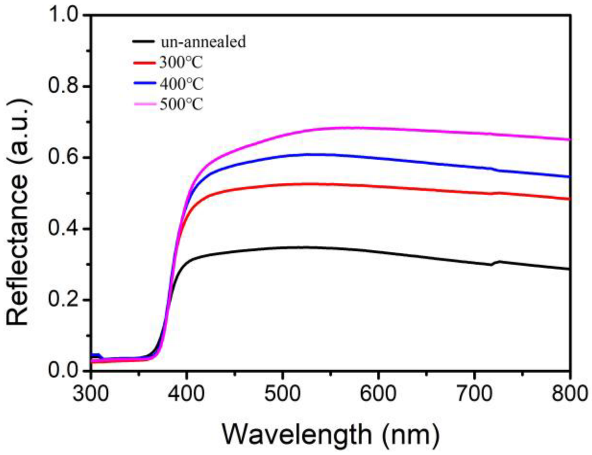

Fig. 4. Optical diffuse-reflectance spectra of laser-ablated ZnO-TiO₂ core-shell nanocomposites annealed at various temperatures.

For further investigating the absorption properties of laser-ablated nanocomposites, the absorption coefficient can be approximated using Kubelka-Munk function *F*(*R)*, which can be determined via following equation (2).

$$F(R) = \frac{(1-R)^2}{2R} \tag{2}$$

where R represents the reflectance recorded by DRS. The optical absorption of laser-ablated ZnO-TiO_2 core-shell nanocomposites subjected to different post-thermal treatment temperatures are depicted in Fig. 5. As shown, the absorption edge positions of nanocomposites subjected to different annealing temperatures exhibit only minor shifts, suggesting that the energy band gap for the fabricated ZnO-TiO_2 core-shell nanocomposites is not significantly affected by changes in annealing temperature.

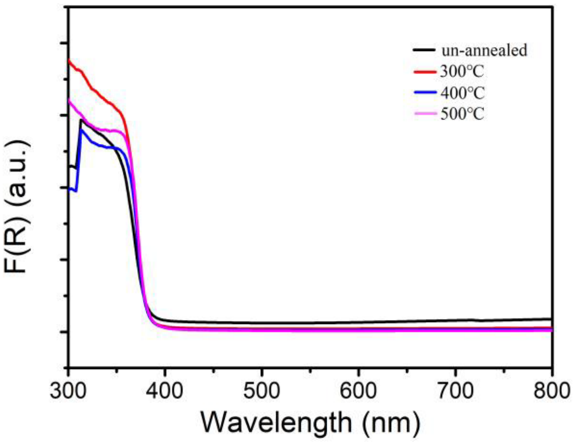

Fig. 5. Absorption of laser-ablated ZnO-TiO₂ core-shell nanocomposites subjected to different annealing temperatures.

The optical band gaps can be further estimated using the Tauc Plot method, as shown in the equation (3).

$$[F(R)hv]^n = \mathrm{A}(hv - E_g) \qquad (3)$$

where A is a proportionality constant, h denotes Planck's constant, v stands for the frequency of incident photons and E_g refers to the semiconductor’s band gap energy. According to the type of transition, the exponent n can be taken a value of 2 or 1/2, corresponding to the direct or indirect allowed transitions, respectively [10]. Tauc plots of $[F(R)hv]^2$ versus energy of photons for LAL-synthesized nanocomposites annealed at different temperatures are displayed in Fig. 6. When the value of $[F(R)hv]^2$ reaches zero, the optical band gaps can be determined from the incident photon energies. By extrapolating linear segment of the curve to the x-axis, the energy band gaps for samples are identified from the intersection points. The band gap energies of laser ablated $ZnO\text{-}TiO_2$ core-shell nanoparticles are determined to be 3.32 eV for non-annealed samples, and 3.31 eV, 3.30 eV, and 3.31 eV for samples annealed at 300 ℃, 400 ℃ and 500 ℃, correspondingly. These optical band gap values fall within the ultraviolet wavelength range, indicating that the synthesized core-shell nanoparticles exhibit excellent ultraviolet responsiveness.

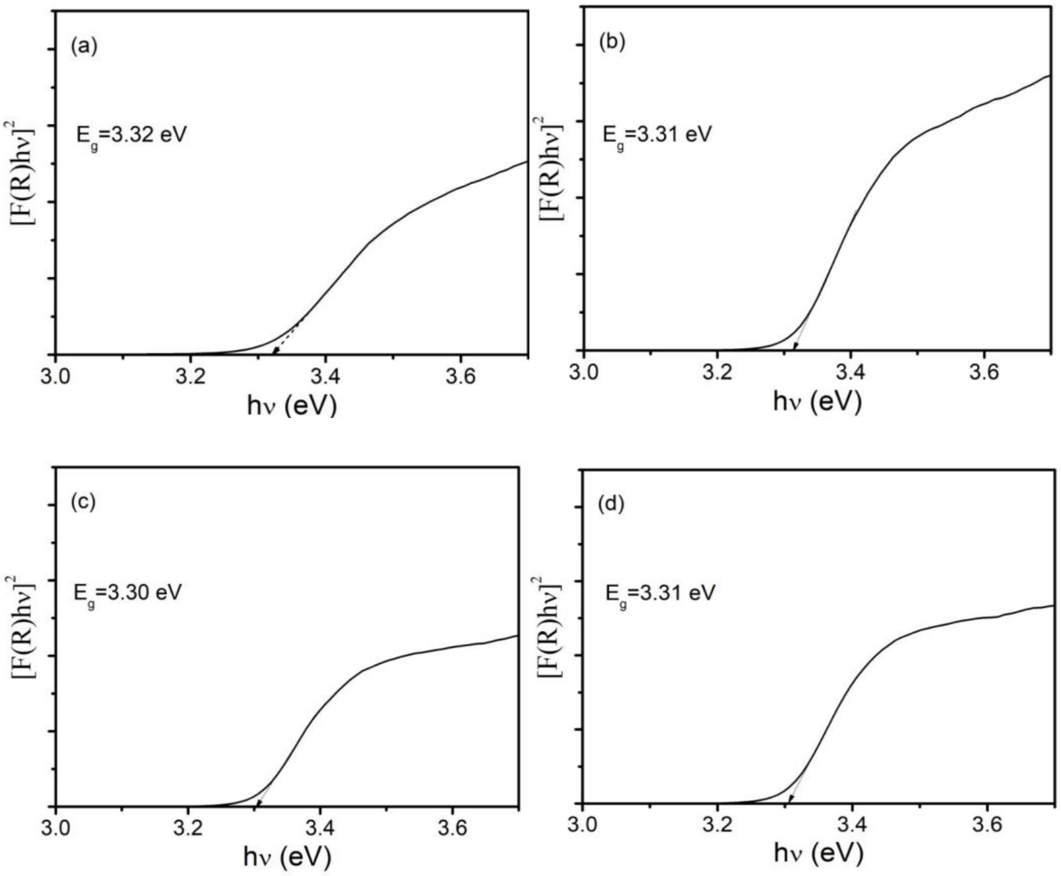

Fig. 6. Plots of $[F(R)hv]^2$ *versus hv for laser-synthesized nanocomposites (a) without annealing, annealed at (b) 300 ℃, (c) 400 ℃, (d)500 ℃.*

The photocatalytic properties of the synthesized core-shell nanocomposites were assessed by monitoring the degradation of RhB dye under ultraviolet light irradiation. As illustrated in Fig. 7, the optical absorption spectra in UV-Vis range for the separated dye solution were recorded at an interval of 30 minutes throughout the photocatalytic process. For all samples, the pronounced decrease in the intensity of the characteristic absorption band at 554 nm was observed as irradiation time increased, indicating efficient photocatalytic degradation of dyes by LAL-synthesized ZnO-TiO_2 core-shell nanocomposites.

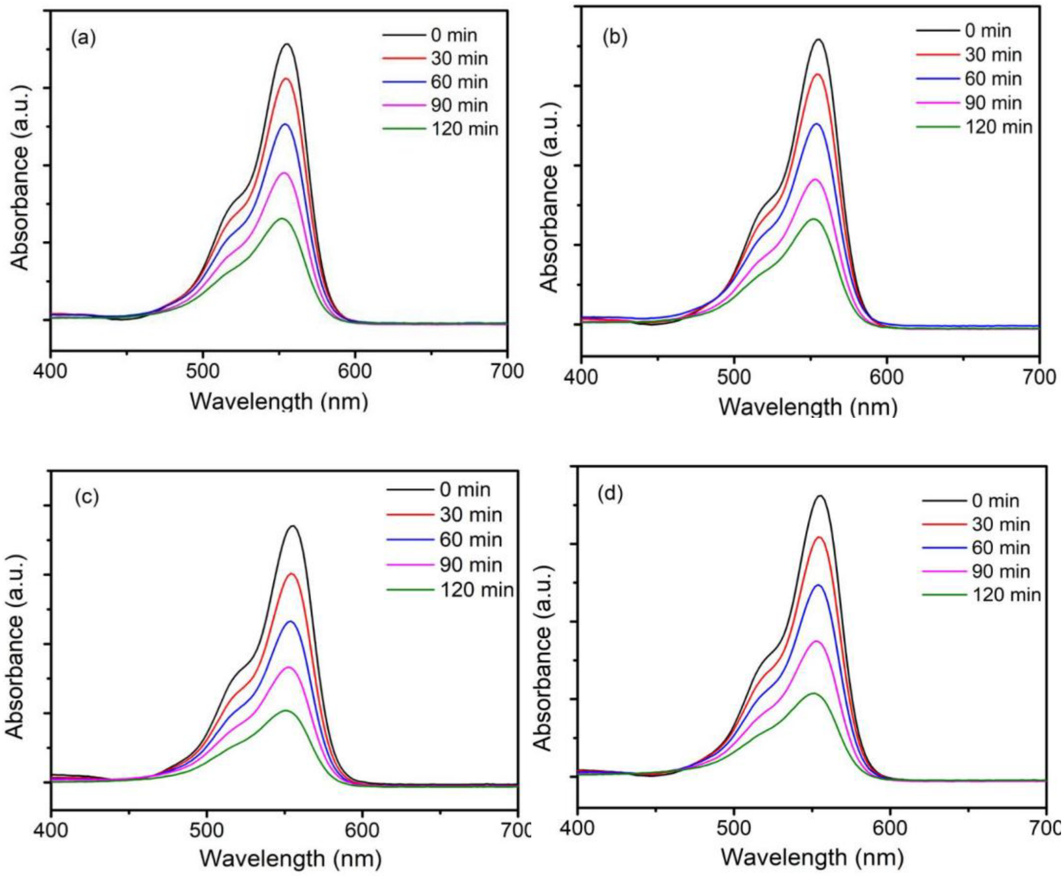

Fig. 7. Optical absorption spectra in UV-Vis range for separated dye solution during photocatalytic process (a)without annealing and annealed at (b) 300 ℃, (c) 400 ℃, (d)500 ℃.

The reduction in the characteristic absorption intensity of RhB dye molecule at 554 nm over time was measured to further evaluate the photocatalytic activity of the nanocomposites. As displayed in Fig.8, the normalized concentrations of dye decrease significantly in the photocatalytic process with a duration of 120 minutes. The normalized concentration versus degradation time curves for the photocatalytic degradation of dyes by nanocomposites subjected to different post-thermal treatments exhibit distinct differences.

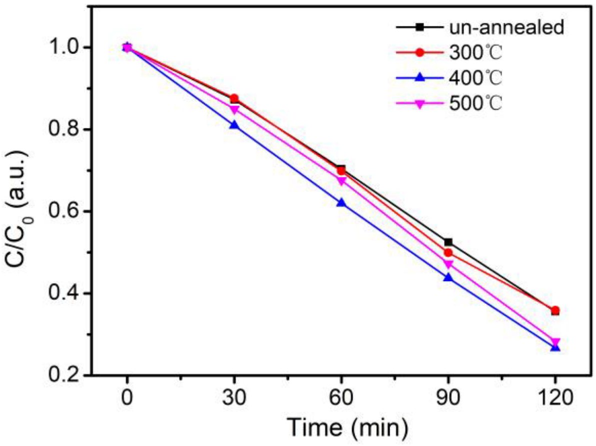

Fig. 8. Normalized concentrations of dye versus degradation time curves.

The efficiency (ŋ) can be accessed as following equation (4).

$$ŋ = \frac{C_0 - C}{C_0} = \frac{A_0 - A}{A_0} = 1 - \frac{A}{A_0} \quad (4)$$

where C and C_0 denote the concentrations of the dye in solution at recorded time and initial time, which can be represented by the corresponding absorbance values of A and A_0, respectively.

For different post-thermal treatments, including un-annealed and annealed at 300 °C, 400 °C, 500 °C, the photocatalytic degradation efficiencies are calculated to 64.4%, 64.1%, 73.3%, 71.7%, respectively

4. Conclusion

In summary, LAL-synthesized ZnO-TiO_2 core-shell nanocomposites exhibited excellent crystallinity, well-defined core-shell morphology, and strong ultraviolet absorption, with only slight variation in optical band gap across annealing conditions. Morphological studies confirm that the composites are nearly spherical with a core-shell architecture, featuring a Zn-rich dense core and an outer shell consisting of ultrasmall TiO_2 nanoparticles, all with sizes below 15 nm. Elemental mapping further validates the distinct spatial distributions of Zn, Ti, and O within the nanocomposites. Photocatalytic tests revealed that post-thermal treatment, particularly annealing at 400 °C, significantly enhances dye degradation efficiency, likely due to optimized structural and defect properties. These findings highlight the potential of such core-shell nanocomposites for advanced UV-driven photocatalytic applications.

Acknowledgements

This work is funded by Guangdong Provincial Key Laboratory of Electronic Functional Materials and Devices (EFMD2024012M), Research Start-up Program of Jinling Institute of Technology (jit-b-202054) and the Key Discipline Construction Project for Physics at Jinling Institute of Technology.

References

[1] Q. Y. Tang, M. J. Yang, S. Y. Yang, Y. H. Xu, Journal of Hazardous Materials 407, 124798 (2021); https://doi.org/10.1016/j.jhazmat.2020.124798

[2] S. Shabn, J. E. Shaji, S. S. J. Dhas, S. Suresh, A. Aravind, S. A. Thomas, V. S. Vinita, J. Samuel, C. S. Biju, Journal of Cluster Science 35, 597-606 (2024); https://doi.org/10.1007/s10876-023-02500-0

[3] A. Alasmari, N. M. Alresheedi, M. A. Alzahrani, F. M. Aldosari, M. Ghasemi, A. Ismail, A. M. Aboraia, Catalysts 14, 946 (2024); https://doi.org/10.3390/catal14120946

[4] J. Guo,Y. H. Sun, Q. Z. Luo, J. Y. Zhang, L. Fang, Environmental Science and Pollution Research 30, 43702-43713 (2023); https://doi.org/10.1007/s11356-023-25276-2

[5] Q. Z. Luo, Y.H. Sun, X. Lv, L. Huang, L. Fang, R. Wang, Journal of Sol-Gel Science and Technology 103, 876-889 (2022); https://doi.org/10.1007/s10971-022-05865-2

[6] J. C. Sin, S. M. Lam, H. H. Zeng, H. Lin, H. X. Li, A. K. Kumaresan, A. R. Mohamed, J. W. Lim, Separation and Purification Technology 250, 117186 (2020); https://doi.org/10.1016/j.seppur.2020.117186

[7] D. M. Xu, H. M.Yu, Y. Qin, Y. Di, H. B. Jia, F. S. Li, J. Li, ACS Applied Nano Materials 7, 2630-2638 (2024); https://doi.org/10.1021/acsanm.3c04783

[8] A. Basaleh, A. A. Ismail, N. Alahmadi, Ceramics International 48, 34273-34282 (2022); https://doi.org/10.1016/j.ceramint.2022.08.004

[9] G. V. Khade, N. L. Gavade, M. B. Suwarnkar, M. J. Dhanavade, K. D. Sonawane,K. M. Garadkar, Journal of Material Science: Material in Electronics 28, 11002-11011 (2017); https://doi.org/10.1007/s10854-017-6883-9

[10] Z. Liu, R. X. Wang, Journal of Ovonic Research 20,455-466 (2024); https://doi.org/10.15251/JOR.2024.204.455

[11] K. L. Reddy, S. Kumar, A. Kumar, V. Krishnan, Journal of Hazardous Materials 367, 694-705 (2019); https://doi.org/10.1016/j.jhazmat.2019.01.004

[12] V. C. Senthilkumar, N. Bhadusha, R. Uthrakumar, K. Kaviyarasu, Journal of Optoelectronic and Biomedical Materials 16, 189-197 (2024); https://doi.org/10.15251/JOBM.2024.164.189

[13] L. A. Al-Hajji, A. A. Ismail, A. Bumajdad, M. Alsaidi, S. A. Ahmed, F. Almutawa, A. Al-Hazza, Ceramics International 46, 20155-20162 (2020); https://doi.org/10.1016/j.ceramint.2020.05.093

[14] V. Bagga, N. Singh, M. Khanuja, M. Rani, D. Kaur, Materials Research Bulletin 159, 112109 (2023); https://doi.org/10.1016/j.materresbull.2022.112109

[15] T. Subramani, S. K. Nagarajan, Ceramics International 50, 34226-34239 (2024); https://doi.org/10.1016/j.ceramint.2024.06.242

[16] J. Y. Yang, Y. L. Zhang, K. Liu, D. X. Tang, S. Z. Zhou, X. J. Yang, Y. S. Li, Y. Liu, Molecules 29, 4342 (2024); https://doi.org/10.3390/molecules29184342

[17] A. Y. Meng, R. Q. Yang, W. Li, Z. Li, J. F. Zhang, Journal of Materiomics 11, 100919 (2025); https://doi.org/10.1016/j.jmat.2024.06.010

[18] P. Kumari, A. Saini, Diksha, J. S. Tawale, P. Prathap, S. K. Srivastava, Journal of Electronic Materials 54, 568-586 (2025); https://doi.org/10.1007/s11664-024-11592-x

[19] S. Ghosh, M. Patel, N. Kumar, J. Lee, J. Lee, C. Choi, D. Zala, A. Ray, J. Kim, Solar RRL 8, 2400384 (2024); https://doi.org/10.1002/solr.202400384

[20] R. Jalal, K. Ozel, A. Atilgan, A Yildiz, Nanotechnology 35, 265705 (2024); https://doi.org/10.1088/1361-6528/ad373b

[21] P. J. Lu, S. W. Fang, W. L. Cheng, S. C. Huang, M. C. Huang, H. F. Cheng, Journal of Food and Drug Analysis 26, 1192-1200 (2018); https://doi.org/10.1016/j.jfda.2018.01.010

[22] D. Nunes, A. Pimentel, L. Santos, P. Barquinha, E. Fortunato, R. Martins, Catalysts 7, 60 (2017); https://doi.org/10.3390/catal7020060

[23] M. A. Gatou, A. Syrrakou, N. Lagopati, E. A. Pavlatou, Reactions 5, 135-194 (2024); https://doi.org/10.3390/reactions5010007

[24] J. J. Li, S. C. Cai , Z. Xu, X. Chen, J. Chen, H. P. Jia, J. Chen, Journal of Hazardous Materials 325, 261-270 (2017); https://doi.org/10.1016/j.jhazmat.2016.12.004

[25] D. Ravikumar, S. C. Jeyakumar, S. S. J. Dhas, C. S. Biju, A. Sivakumar, R. S. Kumar, A. I. Almansour, Materials Science in Semiconductor Processing 173, 108125 (2024); https://doi.org/10.1016/j.mssp.2024.108125

[26] S. Bai, L. M. Wang, X. Y. Chen, J. T. Du, Y. J. Xiong, Nano Research 8, 175-183 (2015); https://doi.org/10.1007/s12274-014-0606-9

[27] Y. Zhang, L. Dou, S. Zhang, X. W. Zheng, S. T. Huang, Materials Research Bulletin 183, 113194 (2025); https://doi.org/10.1016/j.materresbull.2024.113194

[28] S. Song, H. Song, L. M. Li, S. Y. Wang, W. Chu, K. Peng, X. G. Meng, Q. Wang, B. W. Deng, Q. X. Liu, Z. Wang, Y. X. Weng, H. L. Hu, H. W. Lin, T. Kako, J. H. Ye, Nature Catalysis 4, 1032-1042 (2021); https://doi.org/10.1038/s41929-021-00708-9

[29] P. F. Zhou, Y. B. Shen, S. K. Zhao, G. D. Li, B. Y. Cui, D. Z. Wei, Y. S. Shen, Chemical Engineering Journal 407, 126697 (2021); https://doi.org/10.1016/j.cej.2020.126697

[30] A. Chandra, S. Ghosh, R. Sarkar, S. Sarkar, K. K. Chattopadhyay, Chemosphere 352, 141249 (2024); https://doi.org/10.1016/j.chemosphere.2024.141249

[31] M. G. Zhai, Z. Li, R. G. Li, Z. D. Feng, Q. N. Wang, C. B. Zhang, H. B. Chi, N. Ta, C. Li, Journal of Catalysis 443, 115989 (2025); https://doi.org/10.1016/j.jcat.2025.115989

[32] S. C. Yuan, G. C. Yin, T. Zhao, J. Zhang, S. L. Wei, H. N. Zhang, Z. D. Liu, J. K. Zhang, Q. Lu, M. L. Sun, Solid State Sciences 160, 107832 (2025); https://doi.org/10.1016/j.solidstatesciences.2025.107832

[33] N. Morante, G. Viscusi, G. Gorrasi, K. Monzillo, D. Sannino, Journal of Water Process Engineering 69, 106529 (2025); https://doi.org/10.1016/j.jwpe.2024.106529

[34] S. Q. Wang, Z. L. Zhang, W. Y. Huo, X. H. Zhang, F. Fang, Z. H. Xie, J. Q. Jiang, Chemical Engineering Journal 403, 126331 (2021); https://doi.org/10.1016/j.cej.2020.126331

[35] C. C. Li, J. Lei, X. C. Gu, J. Ju, H. Jiang, C. Z. Li, Y. J. Hu, Journal of Cleaner Production 460, 142557 (2024); https://doi.org/10.1016/j.jclepro.2024.142557

[36] V. Balasubramanian, S. Kalpana, R. Anitha, T. S. Senthil, Materials Science in Semiconductor Processing 182, 108732 (2024); https://doi.org/10.1016/j.mssp.2024.108732

[37] R. Radičić, A. Jurov, J. Zavašnik, J. Kovač, V. Brusar, S. Vdović, D. Novko, N. Krstulović, Applied Surface Science 669, 160498 (2024); https://doi.org/10.1016/j.apsusc.2024.160498

[38] M. A. Gondal, A. M. Ilyas, Umair Baig, Ceramics International 42, 13151-13160 (2016); https://doi.org/10.1016/j.ceramint.2016.05.104